Pergamon

Journal of Structural Geology, Vol. 17, No. 11, pp. 1587 to 1599, 1995

0191-8141/95 $9.50 + 0.00

0191-8141(95)00053-4

Determination of position-gradient tensor from strain measurements and its implications for the displacement across a shear zone

GUOWEI ZHANG* and ANDREW HYNES

Department of Earth and Planetary Sciences, McGill University, 3450 University Street, Montreal, Canada H3A 2A7

(*Received* 17 *December* 1993; *accepted in revised form* 21 *April* 1995)

Abstract—A method is proposed for determination of the position–gradient tensor from conventional strain measurements. The position–gradient tensor can be multiplicatively decomposed into two components, left stretch and rotation tensors. The former is readily supplied by field strain data whereas the latter is generally unknown in nature. In order to determine the position–gradient tensor using strain data, it is assumed that structures within a shear zone are symmetric about the plane common to the transport direction and the pole to the shear zone, or alternatively, that the shear strain in the direction parallel to the pole to the shear zone on the plane normal to the transport direction in a parallel-sided shear zone is negligible. With these assumptions, the position–gradient tensor is fully determined from the attitude and principal ratios of the strain ellipsoid determined from field data. This method has been applied to the strain data from deformed fragments in a succession of Late Triassic volcanic breccias abutting a large strike-slip shear zone in north-central British Columbia. The resulting position–gradient tensor is then used to constrain the displacement across the shear zone, suggesting 39% shortening normal to, and dextral displacement of about 1700 m along, the shear zone.

INTRODUCTION

A complete description of the deformation of a coherent body excluding any bulk translation is supplied by the position–gradient tensor **F** (Means 1983, Passchier & Urai 1988, Passchier 1990, 1993, also known as the deformation–gradient tensor, Malvern 1969, Means 1976, 1982, Sanderson 1982, deformation tensor, De Paor 1983, Means 1990, Treagus 1990, Hrouda 1992, or deformation matrix, Flinn 1979, Fossen & Tikoff 1993, Tikoff & Fossen 1993) which includes both a rigid-body rotation and a stretch tensor. Recent descriptions of the polar Mohr circle for two-dimensional situations which is derived from the **F** tensor (De Paor 1981, as referenced by Means 1982, 1983, Allison 1984, De Paor & Means 1984, Passchier & Urai 1988, Passchier 1990, 1993, Treagus 1990, Simpson & De Paor 1993) have demonstrated the potential of this tensor for the study of the rotation of planar and linear features during deformation.

Conventional strain data are generally used only to construct the inverse Cauchy tensor $\mathbf{B}^{-1}$ (cf. Malvern 1969) with respect to the strained state, which does not include any rigid-body rotation and forms the basis for the familiar Mohr diagram in λ'–γ' space. While this tensor and the associated Mohr diagram can provide information about changes in orientation between elements, they provide no information about external rotations. For these, the **F** tensor is required. With the Mohr circle representation for the **F** tensor in polar space (De Paor 1981, Means 1982, 1983, Passchier & Urai 1988, Passchier 1990, 1993, Treagus 1990, Simpson & De Paor 1993), deformation and rotation of lines and planes at a given point can be determined, although the operations are cumbersome for three-dimensional problems (Treagus 1990).

Mohr diagrams for the **F** tensor have not been applied widely in field structural analysis because of difficulties in determination of the **F** tensor in nature. Determination of the **F** tensor in two dimensions through the construction of the polar Mohr circle using deformed vein sets have previously been discussed (e.g. Passchier & Urai 1988, Passchier 1990). In this paper we discuss the determination of the **F** tensor in three dimensions based on strain data obtained from deformed volcanic fragments near a shear zone. We show that, with certain simplifying assumptions, the **F** tensor may readily be determined from conventional strain data. Once the **F** tensor is known, many other features of the shear zone, such as displacement across it, may be calculated.

POSITION–GRADIENT TENSOR AND ITS POLAR DECOMPOSITION

In this section we briefly review, first, the definitions of tensors, their physical meaning and application in characterising geological deformation, and secondly the polar decomposition of the position–gradient tensor.

Considering a particle that moves from $x(x_1, x_2, x_3, t_0)$ in the unstrained state to $x'(x'_1, x'_2, x'_3, t)$ in the strained state, the general relationship between x and x' may be written:

$$\begin{aligned} x'_1 &= x'_1(x_1, x_2, x_3, t) \\ x'_2 &= x'_2(x_1, x_2, x_3, t) \\ x'_3 &= x'_3(x_1, x_2, x_3, t) \end{aligned} \quad (1)$$

*Present address: Department of Geology, University of Toronto, Erindale Campus, Mississauga, ON L5L 1C6, Canada.

where x_i and x_i' (i = 1 to 3) represent the coordinates of the particle in the unstrained and strained states and t represents the time at which the strained state is achieved. If a vector $\mathbf{dx}$, with length ds before deformation is transformed by equation (1) to $\mathbf{dx}'$, with length ds' after deformation, then we have

$$\mathbf{dx}' = \mathbf{F}\mathbf{dx} \tag{2a}$$

or

$$\mathbf{dx} = \mathbf{F}^{-1}\mathbf{dx}' \tag{2b}$$

where $\mathbf{F}$ and $\mathbf{F}^{-1}$ are the position–gradient tensor and its inverse, and

$$\mathbf{F} = \begin{pmatrix} \frac{\partial x_1'}{\partial x_1} & \frac{\partial x_1'}{\partial x_2} & \frac{\partial x_1'}{\partial x_3} \\ \frac{\partial x_2'}{\partial x_1} & \frac{\partial x_2'}{\partial x_2} & \frac{\partial x_2'}{\partial x_3} \\ \frac{\partial x_3'}{\partial x_1} & \frac{\partial x_3'}{\partial x_2} & \frac{\partial x_3'}{\partial x_3} \end{pmatrix}. \tag{3}$$

If the $\mathbf{F}$ tensor in equation (3) is symmetric, it represents irrotational deformation. Otherwise, it represents rotational deformation. Since the deformation history or path of a deformation event is generally not known in nature, we can typically describe only the final configuration of geological structures and relate them to their initial configuration. Consequently, the $\mathbf{F}$ tensor is reduced to the functions which are dependent only on spatial coordinates.

Following equations (2a) and (2b), the length (ds') of the vector $\mathbf{dx}'$ after deformation can be written

$$(ds')^2 = (\mathbf{dx}')^{\mathrm{T}}\mathbf{dx}' = (\mathbf{dx})^{\mathrm{T}}\mathbf{F}^{\mathrm{T}}\mathbf{F}\mathbf{dx} = (\mathbf{dx})^{\mathrm{T}}\mathbf{C}\mathbf{dx} \tag{4a}$$

where $\mathbf{F}^{\mathrm{T}}$ is the transpose of $\mathbf{F}$ and $\mathbf{F}^{\mathrm{T}}\mathbf{F}$ is the Green tensor $\mathbf{C}$ (also known as the right Cauchy-Green tensor, cf. Malvern 1969) with respect to the unstrained state ($\mathbf{dx}$). Similarly, its initial length (ds) is

$$\begin{aligned}(ds)^2 &= (\mathbf{dx})^{\mathrm{T}}\mathbf{dx} = (\mathbf{dx}')^{\mathrm{T}}(\mathbf{F}^{-1})^{\mathrm{T}}\mathbf{F}^{-1}\mathbf{dx}' \\ &= (\mathbf{dx}')^{\mathrm{T}}\mathbf{B}^{-1}\mathbf{dx}'\end{aligned} \tag{4b}$$

where $\mathbf{F}^{-1}$ is the inverse of $\mathbf{F}$ and $(\mathbf{F}^{-1})^{\mathrm{T}}\mathbf{F}^{-1}$ is the inverse of the Cauchy tensor $\mathbf{B}$ (also known as the left Cauchy-Green tensor, cf. Malvern 1969) with respect to the strained state ($\mathbf{dx}'$). It is evident from equations (4a) and (4b) that quadratic elongation of any line in the direction of $\mathbf{dx}$ and reciprocal quadratic elongation of any line in the direction of $\mathbf{dx}'$ can be expressed as

$$\lambda = \mathbf{n}^{\mathrm{T}}\mathbf{C}\mathbf{n} \tag{5a}$$

and

$$\lambda' = (\mathbf{n}')^{\mathrm{T}}\mathbf{B}^{-1}\mathbf{n}' \tag{5b}$$

where $\mathbf{n}$ and $\mathbf{n}'$ are unit column vectors for $\mathbf{dx}$ and $\mathbf{dx}'$, respectively, and $\mathbf{n}^{\mathrm{T}}$ and $\mathbf{n}'^{\mathrm{T}}$ are transposes of $\mathbf{n}$ and $\mathbf{n}'$. When $\mathbf{n}$ and $\mathbf{n}'$ in equations (5a) and (5b) are parallel to the principal directions of the strain state with respect to $\mathbf{dx}$ and $\mathbf{dx}'$ at a given point, $\mathbf{C}$ and $\mathbf{B}^{-1}$ tensors reach their extrema, giving the principal quadratic and reciprocal quadratic elongations. Both $\mathbf{C}$ and $\mathbf{B}^{-1}$ tensors are symmetric.

Generally, the $\mathbf{F}$ tensor can be decomposed into two components; a rigid-body rotation and a stretch tensor (e.g. Malvern 1969, De Paor 1983, Means 1983). In the case of finite strain, the $\mathbf{F}$ tensor can be multiplicatively decomposed into the product of two tensors, one of which represents rigid-body rotation while the other represents 'pure' deformation (e.g. Malvern 1969, De Paor 1983, Means 1983), since the deformation is no longer additive (cf. Malvern 1969). This decomposition is frequently called the polar decomposition (e.g. Malvern 1969, De Paor 1983, Means 1983) and may be written

$$\mathbf{F} = \mathbf{RU} = \mathbf{VR} \tag{6}$$

where $\mathbf{R}$ is rotation tensor, and U and $\mathbf{V}$ are symmetric right and left stretch tensors with respect to $\mathbf{dx}$ and $\mathbf{dx}'$, respectively. Since they are the stretch tensors, $\mathbf{U}$ and $\mathbf{V}$ can be related to quadratic and reciprocal quadratic elongations as follows (see also equations 5a and 5b)

$$\boldsymbol{\lambda} = (\mathbf{P}^{\mathrm{T}}\mathbf{U}\mathbf{P})(\mathbf{P}^{\mathrm{T}}\mathbf{U}\mathbf{P}) = \mathbf{P}^{\mathrm{T}}\mathbf{U}^2\mathbf{P} = \mathbf{P}^{\mathrm{T}}\mathbf{C}\mathbf{P} \tag{7a}$$

and

$$\begin{aligned}\boldsymbol{\lambda}' &= ((\mathbf{P}')^{\mathrm{T}}\mathbf{V}\mathbf{P}')^{-1}((\mathbf{P}')^{\mathrm{T}}\mathbf{V}\mathbf{P}')^{-1} \\ &= (\mathbf{P}')^{\mathrm{T}}(\mathbf{V}^2)^{-1}\mathbf{P}' = (\mathbf{P}')^{\mathrm{T}}\mathbf{B}^{-1}\mathbf{P}'\end{aligned} \tag{7b}$$

where both $\mathbf{P}$ and $\mathbf{P}'$ are unit orthogonal matrices comprising column vectors for three orthogonal directions with respect to $\mathbf{dx}$ and $\mathbf{dx}'$, respectively.

The $\mathbf{B}^{-1}$, or $\mathbf{V}$ tensor (see equation 7b) is the one generally determined directly by routine measurements of strain markers (e.g. deformed oolites, concretions, reduction spots, lapilli, fossils, etc.; e.g. Ramsay 1967, Elliott 1970, Ramsay & Huber 1983) in the field, or indirectly by measuring magnetic fabric (anisotropy of magnetic susceptibility) of strained rocks (e.g. Owens 1974, Rochette 1988, Henry 1990, Hrouda 1992, 1993). Determination of the $\mathbf{U}$ tensor in strained rocks is almost impossible because the principal directions of the reciprocal strain ellipsoid (cf. Jaeger & Cook 1979, Ramsay & Huber 1983) in the unstrained state ($\mathbf{dx}$) are generally not known in nature. Consequently, the right polar decomposition of the $\mathbf{F}$ tensor in equation (6) can rarely be applied to naturally deformed rocks and we concentrate here on the left polar decomposition.

The $\mathbf{R}$ tensor, an orthogonal matrix, rotates three orthogonal material lines at $\mathbf{P}$ to those that are parallel to the principal axes of $\mathbf{V}$ at $\mathbf{P}'$; hence it performs rigid-body rotation of all lines and planes at a given point. The $\mathbf{F}$ tensor can be uniquely determined if both the rotation tensor $\mathbf{R}$ and left stretch tensor $\mathbf{V}$ are known. The $\mathbf{R}$ tensor is also difficult to determine in the field, unless the initial orientations of material lines that are parallel to the principal axes of the strain ellipsoid are known, or the deformation was irrotational (cf. Ramsay 1967, Ramsay & Graham 1970, Ramsay & Huber 1983, Hrouda 1992).

In the next sections, we discuss how to determine the **F** tensor based on strain measurements and simple assumptions concerning the geometry of structure in a shear zone.

DETERMINATION OF LEFT STRETCH TENSOR

We have determined the inverse Cauchy tensor $\mathbf{B}^{-1}$ in a succession of Late Triassic volcanic breccias abutting a large strike-slip shear zone in north-central British Columbia. These volcanic breccias of the Late Triassic Takla Group are compositionally heterogeneous and dominated by sub-angular or sub-rounded fragments of greenish to dark grey clinopyroxene and clinopyroxene–plagioclase porphyries, commonly in a porphyritic matrix with the same composition as the fragments. Progressive straining of the volcanic fragments is well exhibited in an area of about one square kilometre, bounded to the west by a dextral strike-slip shear zone trending approximately 350° and dipping 75° northeast in the McConnell Creek area, north-central B. C. (Fig. 1). The shear zone is brittle–ductile in nature (Ramsay 1980) and displays well-defined S–C fabrics (Berthé *et al.* 1979) and horizontal slickenlines marked by tremolite and calcite fibres, from which its shear sense and shear direction are inferred. The deformed fragments are clearly displayed on a variety of sections with different orientations, allowing detailed strain analysis. According to the apparent aspect ratios and degree of development of foliation, the area has been divided into three domains in the direction normal to the north-northwest trending shear zone (Fig. 1). Domain 1 is about 600 m wide and lies in the east, about 300 m from the shear zone. Domain 2, about 200 m wide, lies between domains 1 and 3, and domain 3 is mainly within the shear zone with a width of about 100 m (Fig. 1). In domain 1, fragments in which phenocrysts or euhedral clinopyroxene and wispy plagioclase are relatively fresh, are slightly deformed (Fig. 2a). Passing westward into domain 2 the strain is more intense, giving rise to a marked increase in the apparent aspect ratios of the deformed fragments (Fig. 2b) and local development of foliation. In domain 3, fragments are very strongly deformed (Fig. 2c), and foliation is penetrative where the phenocrysts of euhedral clinopyroxene have been completely replaced by chlorite and calcite. The deformation of the volcanic fragments is associated with motion along the NNW-trending shear zone, because the aspect ratios of the deformed fragments increase progressively moving from domain 1 to domain 3 (Figs. 2a–c). No deformation occurs east of domain 1.

More than 700 strained volcanic fragments were measured on 60 sections of different orientations in the three domains, of which 20 sections are from domain 1, 32 sections from domain 2 and 8 sections from domain 3 (Table 1). The mean sectional ellipses for all sections in each domain were then standardized with respect to each other (cf. Ramsay & Huber 1983) and used to calculate stretches along the intersections of each section with the three orthogonal planes: horizontal, east–west and north–south vertical (Zhang & Hynes 1994). In the analysis that follows, the sections in each domain are treated as if all sampled the same bulk strain ellipsoid, although there is probably a continuous change in bulk strain-ratio across each domain. In the ideal case, in which all fragments in each domain had the same eccen-

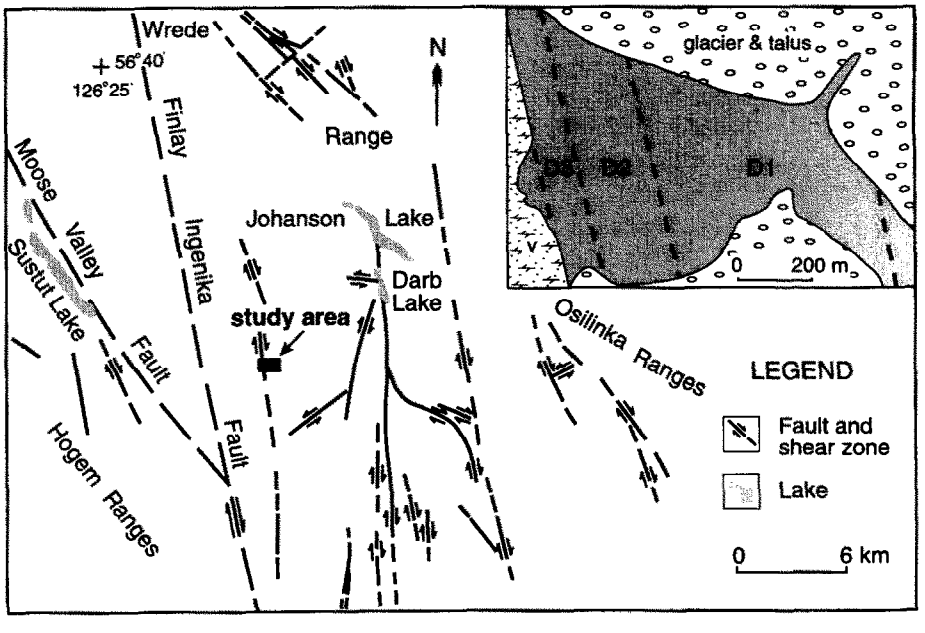

Fig. 1. Simplified structural map of the Johanson Lake area, north-central British Columbia (after Zhang & Hynes 1994), showing the location of the studied shear zone. Insert shows division of domains along the shear zone. Shaded area: outcrop of deformed volcanic breccias; v: vegetation; broken line: approximate boundary between domains; D1, D2 and D3; domains 1, 2 and 3.

tricity, this analysis should provide three perfect ellipses in the three planes for each domain. The strain data within each domain lie approximately in the loci of the ellipses (see figs. 11–13 in Zhang & Hynes 1994), and only two data sets, from domains 1 and 3, respectively, depart significantly from this condition and were not used in further analyses. The least-squares best-fit strain ellipse (Erslev & Ge 1990) was then determined in each of the three planes (Table 1). Finally, components of the $\mathbf{B}^{-1}$ tensor (equation 7b) in geographic space were calculated using the strain ellipses in the three planes (cf. Ramsay 1967, Malvern 1969, Means 1976, Ramsay & Huber 1983), and eigenvalues and eigenvectors of the $\mathbf{B}^{-1}$ tensor were used to determine the axial ratios and directions of the strain ellipsoid for each domain (Table 1 and Fig. 3). Because only two-dimensional strain ratios are known, the values of the principal axes ($1 + e_i$, where $i = 1$ to 3) of the strain ellipsoids (Table 1) have no physical meaning, but their ratios (a and b) can be determined. From the axial ratios a and b (Table 1), it is clear that *L–S* fabrics are predominant in domains 1 and 2 while L fabric characterizes domain 3. In addition, E values (where $E = \ln[(1 + e_1)/(1 + e_3)]$) of domains 1, 2 and 3 are equal to 1.39, 1.57 and 3.70, respectively and fall within the typical strain-anisotropy range of naturally deformed rocks (E is generally less than 4, cf. Pfiffner & Ramsay 1982, Hrouda 1993).

In the following analysis, it is assumed that the volcanic fragments experienced a constant volume deformation as features due to the volume change, such as pressure solution, are absent, and absolute values for the principal axes of the strain ellipsoid are given in Table 2. Here, we also define two coordinate systems: geographic and shear space. In geographic space, we take axis x_g north horizontal, y_g east horizontal and z_g pointing to the centre of Earth. In shear space, axis x_s is set parallel to the slickenlines on the shear surface of the footwall, pointing in the shear direction of the hanging wall, y_s is normal to the shear surface pointing towards the hanging wall and z_s is perpendicular to x_s and y_s lying in the shear surface (Fig. 4). Both coordinate systems are right-handed.

As the deformation within each domain is treated as homogeneous, the general transformations (1) become linear coordinate transformations. Based on equation (6), the position–gradient tensor **F** can be decomposed into a left stretch and a rigid-body rotation tensor in shear space:

$$\begin{pmatrix} F_{xx} & F_{xy} & F_{xz} \\ F_{yx} & F_{yy} & F_{yz} \\ F_{zx} & F_{zy} & F_{zz} \end{pmatrix} = \begin{pmatrix} V_{xx} & V_{xy} & V_{xz} \\ V_{yx} & V_{yy} & V_{yz} \\ V_{zx} & V_{zy} & V_{zz} \end{pmatrix} \begin{pmatrix} R_{xx} & R_{xy} & R_{xz} \\ R_{yx} & R_{yy} & R_{yz} \\ R_{zx} & R_{zy} & R_{zz} \end{pmatrix} \quad (8)$$

where F_{ij} are independent of position. Furthermore, from equation (7b), the left stretch tensor V_{ij} can be expressed as:

$$\begin{pmatrix} V_{xx} & V_{xy} & V_{xz} \\ V_{yx} & V_{yy} & V_{yz} \\ V_{zx} & V_{zy} & V_{zz} \end{pmatrix} = (\mathbf{P}'_s)^T \mathbf{P}'_g \begin{pmatrix} 1+e_1 & 0 & 0 \\ 0 & 1+e_2 & 0 \\ 0 & 0 & 1+e_3 \end{pmatrix} (\mathbf{P}'_g)^T \mathbf{P}'_s \quad (9)$$

where $1 + e_i$ is the ith principal stretch, $\mathbf{P}'_g$ comprises the principal directions of the strain ellipsoid in geographic space and $\mathbf{P}'_s$ specifies the directions of the coordinate axes of shear space in geographic space. Since $\mathbf{P}'_g$ and $1 + e_i$ are known from the strain analysis (Fig. 3 and Table 2) and $\mathbf{P}'_s$ is obtained from the attitudes of the slickenline and the shear zone (Fig. 3), the values of V_{ij} are fully specified by this equation. The resulting **V** tensors for domains 1, 2 and 3 are shown in equations 10(a–c).

$$\mathbf{V}^{(1)} = \begin{pmatrix} 1.8027 & 0.2061 & 0.0780 \\ 0.2061 & 0.5015 & -0.0803 \\ 0.0780 & -0.0803 & 1.1807 \end{pmatrix} \quad (10a)$$

$$\mathbf{V}^{(2)} = \begin{pmatrix} 1.8772 & 0.3396 & -0.0218 \\ 0.3396 & 0.4873 & -0.0068 \\ -0.0218 & -0.0068 & 1.2510 \end{pmatrix} \quad (10b)$$

$$\mathbf{V}^{(3)} = \begin{pmatrix} 7.7193 & 2.5497 & 0.1942 \\ 2.5497 & 1.0794 & 0.0732 \\ 0.1942 & 0.0732 & 0.5511 \end{pmatrix}. \quad (10c)$$

DETERMINATION OF POSITION–GRADIENT TENSOR

The rotation tensor R_{ij} may be expanded, without loss of generality, into

$$\begin{pmatrix} R_{xx} & R_{xy} & R_{xz} \\ R_{yx} & R_{yy} & R_{yz} \\ R_{zx} & R_{zy} & R_{zz} \end{pmatrix} = \begin{pmatrix} \cos\omega_z & \sin\omega_z & 0 \\ -\sin\omega_z & \cos\omega_z & 0 \\ 0 & 0 & 1 \end{pmatrix} \times \begin{pmatrix} \cos\omega_y & 0 & \sin\omega_y \\ 0 & 1 & 0 \\ -\sin\omega_y & 0 & \cos\omega_y \end{pmatrix} \begin{pmatrix} 1 & 0 & 0 \\ 0 & \cos\omega_x & \sin\omega_x \\ 0 & -\sin\omega_x & \cos\omega_x \end{pmatrix} \quad (11)$$

where ω_x, ω_y and ω_z are rotational angles about coordinate axes x_s, y_s and z_s and the order of rotations is that ω_x takes place first followed sequentially by ω_y and ω_z. In order to calculate the **F** tensor, the rigid-body rotational angles (ω_x, ω_y and ω_z) and their order of rotations must be known.

In the studied region, observed strain ellipsoids are symmetric to the plane that is common to the slickenline (x_s) and pole to the shear zone (y_s) (see Fig. 3), which is a common feature of shear zones (Ramsay & Graham 1970, Twiss and Gefell 1990). It follows that rotational angles ω_x and ω_y must be zero. Setting ω_x and ω_y to zero in equation (11) and then substituting equations (9) and

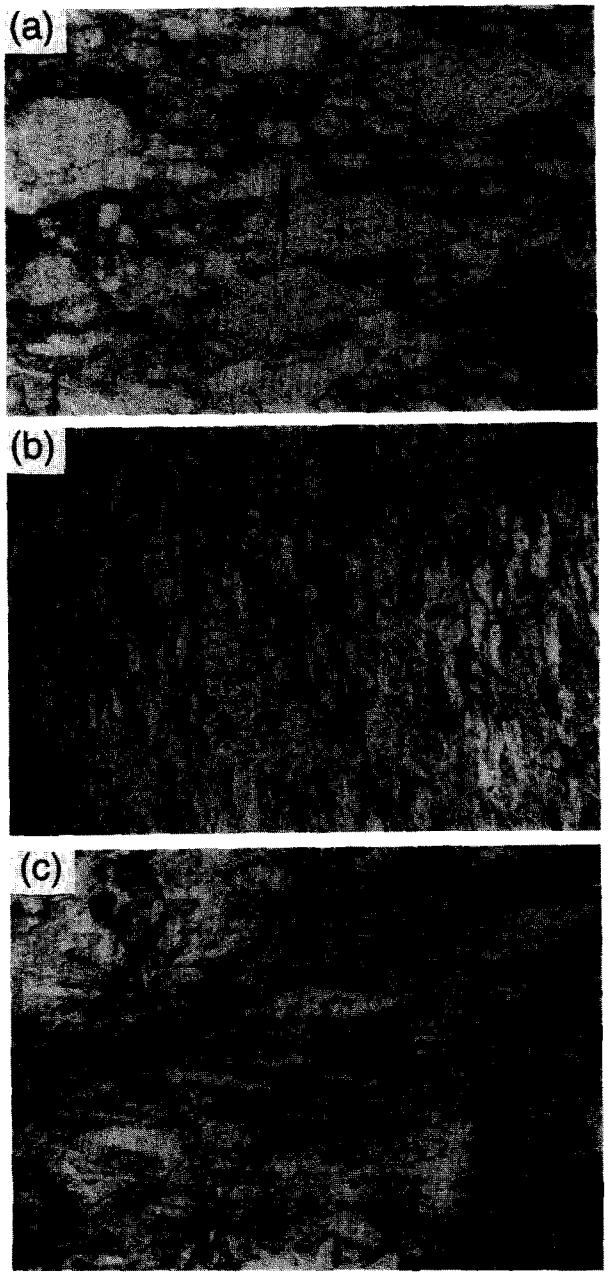

Fig. 2. Deformed volcanic breccia fragments along the shear zone. (a) from domain 1, pencil pointing southwest; (b) from domain 2, pencil pointing southeast; (c) from domain 3, pencil pointing southeast. All these three sections are subhorizontal.

Table 1. Strain data from deformed volcanic fragments

Domain	Plane	A	B	α (°)	$1 + e_i$	Trend (°)	Plunge (°)	a	b	n_s	n_f
1	NE	3.73	1.00	160.6	3.785	343.3	7.6	1.552	2.589	19	170
	EW	2.54	1.03	66.8	2.438	091.3	66.6				
	NS	2.78	1.62	54.8	0.942	250.2	22.0				
2	NE	4.73	1.02	156.6	4.732	336.9	1.6	1.565	3.058	32	512
	EW	3.05	1.07	73.9	3.024	072.8	75.2				
	NS	3.24	1.86	40.6	0.989	246.5	14.7				
3	NE	17.84	0.91	151.0	35.740	332.2	6.2	15.736	2.560	7	58
	EW	2.23	0.99	75.1	2.271	087.2	75.5				
	NS	2.92	1.59	44.7	0.887	240.8	13.0				

Notes: NE, EW and NS: horizontal, east–west and north–south vertical plains; A and B: long and short axes of the least-squares best-fit strain ellipses in the above planes; α: angle between long axis of the strain ellipse and coordinate axis (e.g. north, east and down in NE, EW and NS planes, respectively); $1 + e_i$, where i = 1–3: values of long, intermediate and short axes of the strain ellipsoid; trend/plunge: direction of the corresponding axis of the strain ellipsoid; $a = (1 + e_1)/(1 + e_2)$; $b = (1 + e_2)/(1 + e_3)$; n_s: number of sections used; n_f: number of fragments measured (see Zhang & Hynes 1994 for details).

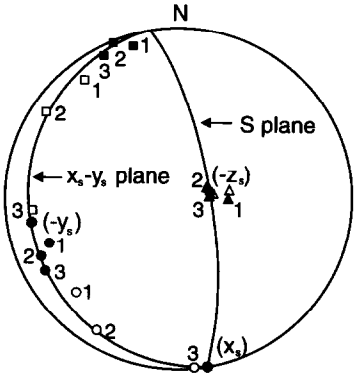

Fig. 3. Stereographic plot of principal directions of the observed strain ellipsoids from domains 1, 2 and 3. Squares, triangles and circles: long, intermediate and short axes of the observed strain ellipsoids in the strained state (solid) and their corresponding material lines (unfilled) in the unstrained state (determined through unrotation by the **R** tensors in equation 16); S plane: shear plane; number: showing domain; grey circles: directions of the coordinate axes (x_s, y_s and z_s) of shear space in Fig. 4. All stereograms are lower-hemisphere, equal area projections. The observed strain ellipsoids are symmetric about the x_s–y_s plane.

(11) into (8), the relationships in equation (8) can be simplified to:

$$\begin{pmatrix} F_{xx} & F_{xy} & F_{xz} \\ F_{yx} & F_{yy} & F_{yz} \\ F_{zx} & F_{zy} & F_{zz} \end{pmatrix} = \begin{pmatrix} V_{xx}\cos\omega_z - V_{xy}\sin\omega_z & V_{xx}\sin\omega_z + V_{xy}\cos\omega_z & V_{xz} \\ V_{yx}\cos\omega_z - V_{yy}\sin\omega_z & V_{yx}\sin\omega_z + V_{yy}\cos\omega_z & V_{yz} \\ V_{zx}\cos\omega_z - V_{zy}\sin\omega_z & V_{zx}\sin\omega_z + V_{zy}\cos\omega_z & V_{zz} \end{pmatrix} \quad (12)$$

The symmetry of structures within a shear zone requires not only that the rotational angles ω_x and ω_y equal zero but also that the shear components F_{xz}, F_{yz}, F_{zx} and F_{zy} in equation (12) be zero, as pointed out by Ramsay and Graham (1970). Consequently, equation (12) may be simplified to:

$$\begin{pmatrix} F_{xx} & F_{xy} & 0 \\ F_{yx} & F_{yy} & 0 \\ 0 & 0 & F_{zz} \end{pmatrix} = \begin{pmatrix} V_{xx}\cos\omega_z - V_{xy}\sin\omega_z & V_{xx}\sin\omega_z + V_{xy}\cos\omega_z & 0 \\ V_{yx}\cos\omega_z - V_{yy}\sin\omega_z & V_{yx}\sin\omega_z + V_{yy}\cos\omega_z & 0 \\ 0 & 0 & V_{zz} \end{pmatrix} \quad (13)$$

Now we have 5 independent equations for 6 unknowns F_{xx}, F_{xy}, F_{yx}, F_{yy}, F_{zz} and ω_z, and the components F_{ij} are still indeterminate without other structural information. Below we discuss methods through which this other information may be supplied.

General deformation

As a simple working hypothesis, provided several positions on the strain path are known, and provided the strain path results from progressive increments of strain in response to constant kinematics, it may be possible to determine the **F** tensor through forward modelling, searching for the incremental tensor $\mathbf{F}_i$ whose characteristics best account for the observed points along the strain path. The requirement of a successful forward model is that it reproduces the strain path, as illustrated on strain diagrams like that of Fig. 5, and that both the orientations and values of the principal axes of the modelled strain ellipsoids correspond within reasonable limits to those actually observed. With a computer, such forward modelling, and the automatic searching for a viable solution, is a fairly straightforward procedure.

The methods for calculating progressive strain paths have previously been discussed by a number of workers (e.g. Ramsay 1967, Ramberg 1975, Flinn 1979, Sanderson & Marchini 1984, Weijermars 1991, Fossen & Tikoff 1993). In our approach, the strain path is derived by successive multiplication by the incremental $\mathbf{F}_i$ tensor:

$$\mathbf{F}_1 = \mathbf{F}_i;\ \mathbf{F}_2 = \mathbf{F}_1\mathbf{F}_i;\ \mathbf{F}_3 = \mathbf{F}_2\mathbf{F}_i;\ \ldots;\ \mathbf{F}_n = \mathbf{F}_{n-1}\mathbf{F}_i. \quad (14)$$

In the following analysis, only constant volume deformation is considered.

Progressive irrotational strains for constant kinematics have been discussed (e.g. Ramsay 1967, Ramberg 1975, Flinn 1979) and the strain paths in ln a–ln b space are all straight lines (Ramsay 1967). For progressive rotational strain, all strain paths in ln a–ln b space for any

Table 2. The observed and calculated strain ellipsoids

Domain	Observed 1 + e_i	Observed Trend (°)	Observed Plunge (°)	Calculated 1 + e_i	Calculated Trend (°)	Calculated Plunge (°)	d_i (%)	α_i (°)
1	1.841	343.3	7.6	1.835	341.5	2.3	0.3	5.7
	1.186	091.3	66.6	1.181	080.0	75.0	0.4	9.2
	0.458	250.2	22.0	0.470	250.9	14.8	2.5	7.2
2	1.956	336.9	1.6	1.956	337.4	3.3	0.0	1.8
	1.250	072.8	75.2	1.251	080.0	75.0	0.1	1.9
	0.409	246.5	14.7	0.409	246.5	14.6	0.0	0.1
3	8.591	332.2	6.2	8.585	331.8	4.8	0.1	1.5
	0.546	087.2	75.5	0.551	080.0	75.0	1.0	1.9
	0.213	240.8	13.0	0.213	240.6	14.2	0.1	1.2

Notes: the observed strain ellipsoids are determined using the sectional strain data in Table 1, whereas the calculated strain ellipsoids are derived using the **F** tensors in equation (15); d_i is the percentage of departure of the axis magnitude (i) of the calculated ellipsoid from that of the observed and α_i is the angle between the axes (i) of the observed and calculated strain ellipsoids, where i = 1–3. Other abbreviations as for Table 1.

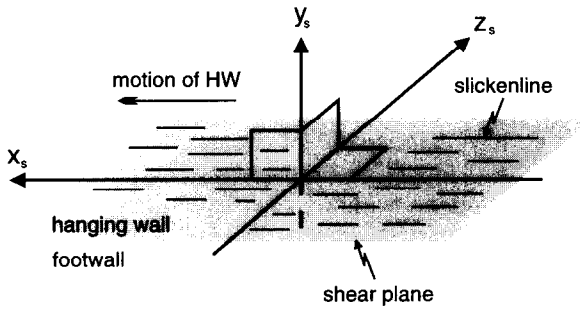

Fig. 4. Diagram showing the choice of coordinate system in shear space. x_s, y_s and z_s: coordinate axes in shear space; HW: hanging wall.

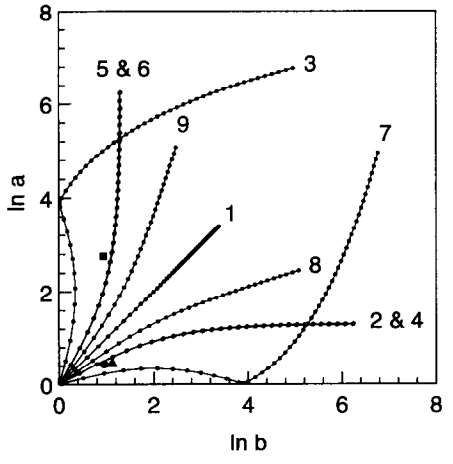

Fig. 5. Plot of shapes of the strain ellipsoids. Solid circle, triangle and square: the observed strain ellipsoids from domains 1, 2 and 3, respectively; dots: the modelled strain ellipsoids; a and b: as for Table 1. The strain ellipsoids of the first and every tenth strain increment are plotted for each strain path; number shows the strain path.

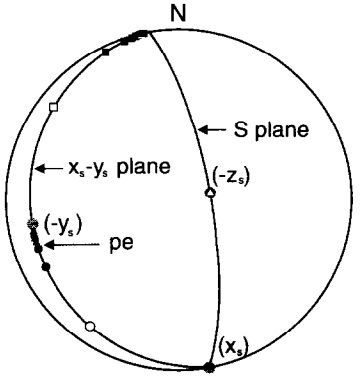

Fig. 6. Stereographic plot of principal axes of the strain ellipsoids for path 3 (Fig. 5). The strain ellipsoids of the first and every fiftieth increment are plotted. Open square, triangle and circle: long, intermediate and short axes of the strain ellipsoid of the first incremental strain, respectively; pe: the prolate ellipsoid (at 114 incremental strain, Fig. 5); other symbols as for Fig. 3. Note that the modelled strain ellipsoids in this, and the following, figure are also symmetric about the x_s–y_s plane.

$\mathbf{F}_i$ tensors are curved except those for plane strain even if the kinematics are constant. This is because the non-zero shear components F_{xy} and F_{yx} contribute to the values of 1 + e_i, so that the simple relationship of $a = b^K$, where $K = \ln[(1 + e_1)/(1 + e_2)]/\ln[(1 + e_2)/(1 + e_3)]$ (cf. Ramsay 1967), is no longer valid.

Figure 5 shows the strain paths for progressive simple shear (path 1) and simple shear combined with (1) shortening along one axis (e.g. y_s, z_s and x_s for paths 2, 3 and 4, respectively) and equal extension along the other two axes, (2) extension along one axis (e.g. x_s, y_s and z_s for paths 5, 6 and 7, respectively) and equal shortening along the other two axes, and (3) unequal extension along all three axes (e.g. paths 8 and 9). The corresponding $\mathbf{F}_i$ tensors are given in the Appendix. With progressive strain, strain ellipsoids starting in the apparent flattening field ($\ln a < \ln b$) change progressively toward oblate ellipsoids, giving rise to upward-convex strain paths (see paths 2, 4 and 8, Fig. 5), whereas those starting in the apparent constrictional field ($\ln a > \ln b$) change progressively toward prolate ellipsoids, displaying upward-concave strain paths (see paths 5, 6 and 9, Fig. 5). This is, however, not true for paths 3 and 7 (see also Fossen & Tikoff 1993), which characterize simple shear combined with equal extension along x_s and y_s and shortening along z_s (equation A3) and with shortening along x_s and y_s and extension along z_s (equation A7). The reason for this is that the shapes of the strain ellipsoids on path 3 before reaching perfect prolateness (Fig. 5) are governed mainly by the shear component F_{xy} (equation A3) as indicated by the fact that the axes of 1 + e_3 lie in the x_s–y_s plane (Fig. 6; note that there is an

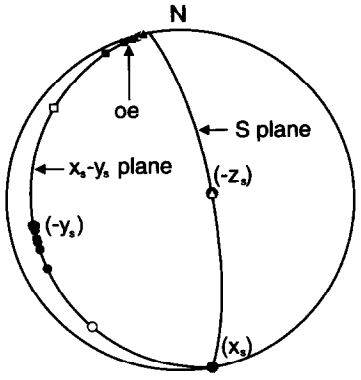

Fig. 7. Stereographic plot of principal axes of the strain ellipsoids for path 7 (Fig. 5); oe: the oblate ellipsoid (at 114 incremental strain, Fig. 5); other symbols as for Fig. 6.

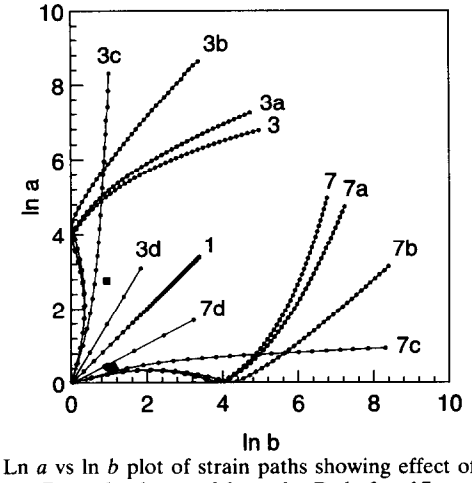

Fig. 8. Ln a vs ln b plot of strain paths showing effect of the shear component F_{yx} on the shapes of the paths. Paths 3 and 7 are the same as those in Fig. 5. F_{yx} = 0.0001, 0.0006, 0.0060 and 0.0604 for (a), (b), (c) and (d), respectively; values of other components of $\mathbf{F}_i$ are same as for paths 3 and 7 (equations A3 and A7), respectively.

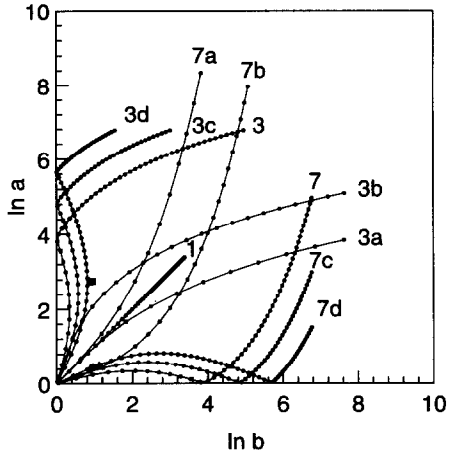

Fig. 9. Ln a vs ln b plot of strain paths showing effect of ratios of F_{xx}/F_{zz} and F_{zz}/F_{xx} on the shapes of the paths. Paths 3 and 7 are same as those in Fig. 5. For paths 3a–d, the ratios of F_{xx}/F_{zz} are 1.090, 1.049, 1.013 and 1.010, respectively; F_{xy} and F_{yx} are same as for path 3 (equation A3). For paths 7a–d, the ratios of F_{zz}/F_{xx} are 1.097, 1.051, 1.013 and 1.010, respectively; F_{xy} and F_{yx} are same as for path 7 (equation A7).

abrupt change of orientation of 1 + e_3 when ln b = 0), whereas subsequent ones are dominated by the stretch components F_{xx}, F_{yy} and F_{zz} (equation A3), as the axes of 1 + e_3 are parallel to z_s (Fig. 6). Similarly, the shapes of strain ellipsoids on path 7 before reaching perfect oblateness (Fig. 5) are governed by F_{xy} (equation A7), whereas subsequent ones are dominated by F_{xx}, F_{yy} and F_{zz} (Fig. 7).

The paths of Fig. 5 are representative of all the general styles of path that can be generated through progressive deformation under conditions of constant kinematics, although the paths can of course vary according to the values of F_{ij}. Increasing the shear component F_{yx} straightens the strain paths. For example, increasing F_{yx} from 0 to $F_{yx} = F_{xy}$, moves the resulting strain paths from 3 and 7 in Fig. 5 progressively to 3d and 7d of Fig. 8, respectively, which are the straight lines characteristic of irrotational strain. Increasing F_{xx}/F_{zz} moves path 3 in Fig. 5 to paths 3a and 3b of Fig. 9. Decreasing the ratio changes path 3 in Fig. 5 to paths 3c and 3d of Fig. 9. Similarly, if the ratio of F_{zz}/F_{xx} increases, path 7 in Fig. 5 will change to paths 7a and 7b (Fig. 9); if the ratio decreases, path 7 will change to paths 7c and 7d (Fig. 9).

None of the progressive strain paths illustrated on Figs. 5, 8 and 9 crosses the plane strain path (path 1, Figs. 5, 8 and 9), from the flattening to the constrictional field or vice versa, for low values of either ln a or ln b, a requirement that would be necessary for a strain path for our strain data. It appears, therefore, that our strain data cannot be explained through a progressive shear model like those presented here. The reason for this is probably that the rocks within the shear zone were involved in a progressive strain of variable kinematics during the deformation. We have not pursued forward modelling further, because we have no means by which to choose among these various possibilities.

Simple shear combined with extension parallel to the coordinate axes

An alternative approach to this problem is based on the mode of deformation, which is frequently observed from field studies (Ramsay & Graham 1970, Ramsay 1980, Sanderson 1982). Since displacement along the slickenline direction is predominant in shear zones bounded by parallel planes of relatively large extent, shear strain (γ_{yx}) along y_s in the plane normal to x_s is small compared with unity (Ramsay & Graham 1970, Ramsay 1980, Sanderson 1982), and, to a first approximation, it can be neglected. This leads to $F_{yx} = 0$, and hence $Vyx \cos \omega_z - V_{yy} \sin \omega_z = 0$ (see equation 13). We then have the relationship $\tan \omega_z = V_{yx}/V_{yy}$. Substituting ω_z into equation (13), the **F** tensor can be determined by the left stretch tensor **V** alone. **F** and **R** tensors for each domain were calculated in this way and they are shown in equations (15) and (16):

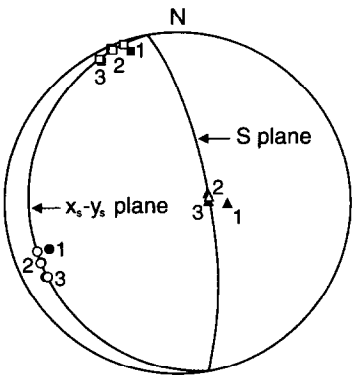

Fig. 10. Stereographic plot of principal axes of the strain ellipsoids from domains 1, 2 and 3. Open squares, triangles and circles: long, intermediate and short axes of the calculated strain ellipsoids (derived using the **F** tensors in equation 15); other symbols as for Fig. 3.

$$\mathbf{F}^{(1)} = \begin{pmatrix} 1.5891 & 0.8758 & 0.0000 \\ 0.0000 & 0.5422 & 0.0000 \\ 0.0000 & 0.0000 & 1.1807 \end{pmatrix} \quad (15a)$$

$$\mathbf{F}^{(2)} = \begin{pmatrix} 1.3460 & 1.3518 & 0.0000 \\ 0.0000 & 0.5940 & 0.0000 \\ 0.0000 & 0.0000 & 1.2510 \end{pmatrix} \quad (15b)$$

$$\mathbf{F}^{(3)} = \begin{pmatrix} 0.6616 & 8.1025 & 0.0000 \\ 0.0000 & 2.7687 & 0.0000 \\ 0.0000 & 0.0000 & 0.5511 \end{pmatrix} \quad (15c)$$

$$\mathbf{R}^{(1)} = \begin{pmatrix} 0.9250 & 0.3801 & 0.0000 \\ -0.3801 & 0.9250 & 0.0000 \\ 0.0000 & 0.0000 & 1.0000 \end{pmatrix} \quad (16a)$$

$$\mathbf{R}^{(2)} = \begin{pmatrix} 0.8205 & 0.5717 & 0.0000 \\ -0.5717 & 0.8205 & 0.0000 \\ 0.0000 & 0.0000 & 1.0000 \end{pmatrix} \quad (16b)$$

$$\mathbf{R}^{(3)} = \begin{pmatrix} 0.3899 & 0.9209 & 0.0000 \\ -0.9209 & 0.3899 & 0.0000 \\ 0.0000 & 0.0000 & 1.0000 \end{pmatrix} \quad (16c)$$

where the superscripts show the domain numbers.

The strain ellipsoids for the three domains were calculated based on the **F** tensors in equation (15) (see Table 2 and Fig. 10). Errors in values of the corresponding principal axes of the observed and calculated strain ellipsoids are all less than 3% (Table 2) and angles between the corresponding principal axes are less than 10° in domain 1 and 2° in domains 2 and 3 (Table 2 and Fig. 10). This indicates that the errors from the assumption that components F_{xz}, F_{zx}, F_{yz} and F_{zy} equal zero are not significant. The strongest support for the validity of the assumption comes from the values of V_{xz}, V_{zx}, V_{yz} and V_{zy} (equation 10) calculated from the strain data. Since these values are all much less than unity, and since they are the sole contributors to the values of F_{xz}, F_{zx}, F_{yz} and F_{zy} (equation 12), these components of **F** could not be large.

Two-dimensional polar Mohr circles of the **F** tensors for domains 1 (equation 15a), 2 (equation 15b) and 3 (equation 15c) are plotted in Figs. 11, 12 and 13, respectively. It can be seen from Figs. 11–13 that the deformation in the shear zone is predominantly in the x_s–y_s plane. Passing from domain 1 to domain 2 there is a slight increase in the deviatoric character of the strain in x_s–y_s and in the rigid-body rotational angle ω_z (see also equation 16, where $R_{xy} = \sin \omega_z$). Passing from domain 2 to domain 3 there is, however, a very large increase in both. In the y_s–z_s plane there is only minor deviatoric strain and in the z_s–x_s plane almost none. These characteristics are similar to those of progressive simple shear, but in true simple shear there is only one set of lines (parallel to the shear zone) that does not rotate, so that the eigenvectors (with unity eigenvalues) in the x_s–y_s plane coincide and the Mohr circle is tangential to the reference axis. This condition is not satisfied for any of the domains (see Figs. 11–13); their Mohr circles in x_s–y_s cut the reference axis, indicating that there was a component of flattening onto the shear plane in this region and that the shear zone is then, broadly speaking, transpressional. The dextral, transpressive character of the shear zone is consistent with other geological structures observed in the region (Zhang & Hynes 1994).

IMPLICATIONS FOR DISPLACEMENT ACROSS THE SHEAR ZONE

F tensors for the three domains were derived by assuming that there had been no shear strain in the direction parallel to the pole to the shear zone on the plane normal to the slickenline ($F_{yx} = 0$). The coordinate axes of shear space after deformation $x'(F_{xx}, 0, 0)$ and $z'(0, 0, F_{zz})$ are parallel to their corresponding initial axes $x(1, 0, 0)$ and $z(0, 0, 1)$. The **F** tensor therefore provides direct estimates of the strain on planes that were approximately parallel to the boundaries of the domains throughout the deformation, and the magnitudes of the diagonal terms correspond approximately to the longitudinal strains $(1 + e_i)$ in planes parallel to these boundaries. Thus, it can be seen (equation 15) that in domains 1 and 2 there was considerable stretching parallel to the boundaries (F_{xx}, $F_{zz} > 1$) and shortening perpendicular to them, but the opposite is true in domain 3. While this difference may be accentuated by an overestimate of the eccentricity of the strain ellipsoid in domain 3, its existence is not in doubt. It is clear that such a marked strain discontinuity requires that the kinematics changed across the boundary between domains 2 and 3 during the progressive deformation and that the boundary was not coherent on the scale of tens of metres. This observation is consistent with the brittle–ductile character of the shear zone, especially along the boundary zone between domains 2 and 3. This strain discontinuity may therefore indicate a switch of kinematics from transpression to transtension (see below) during the progressive deformation.

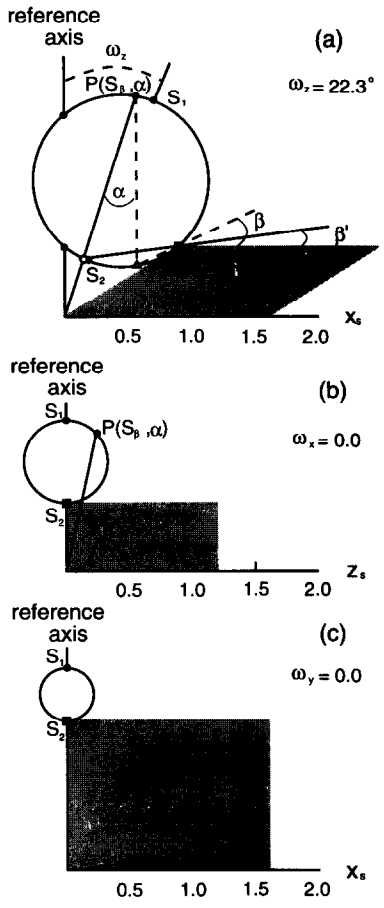

Fig. 11. Polar Mohr circles for domain 1 in (a) x_s–y_s, (b) y_s–z_s, (c) z_s–x_s planes in shear space. The reference axis represents directions of non-rotation in Mohr space. The shaded area represents the deformed unit square in the plane. Solid square represents the anchor point of the deformed pole to the shear zone in both Mohr space and shear space; solid circles (on the reference axis): the eigenvectors of the two-dimensional F tensor in the plane; S_β and α: stretch and rotational angle of a line; β and β': the orientation of a line with respect to the shear zone (the slickenline direction) in the strained and unstrained states, respectively; S_1 and S_2: maximum and minimum principal stretches, respectively, in the plane; ω_z, ω_x and ω_y: rigid-body rotational angles about axes z_s, x_s and y_s, respectively. (See Simpson & De Paor, 1993, for more detailed description of the polar Mohr circle).

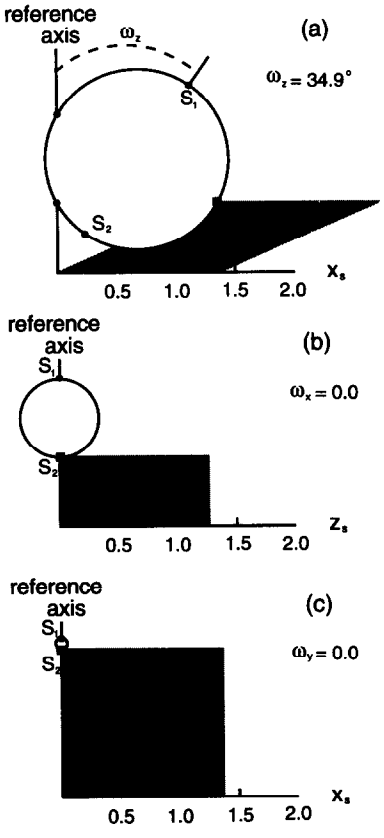

Fig. 12. Polar Mohr circles for domain 2 in (a) x_s–y_s, (b) y_s–z_s, (c) z_s–x_s planes in shear space. Legend as for Fig. 11.

The total amount of shortening normal to the boundaries across domains 1 and 2 is about 507 and 137 m, respectively (the shortening across a domain is equal to $(1/F_{yy} - 1)$ times the final width of the domain (for the values of F_{yy} see equations 15a & b)), and the total extension normal to the shear plane across the domain 3 is about 64 metres (the extension across a domain is equal to $(1 - 1/F_{yy})$ times the final width of the domain (for the value of F_{yy} see equation 15c)). Total shortening normal to the shear zone is therefore 580 m over 1480 m, about 39% shortening. Cumulative dextral displacement along the shear zone is about 1700 m (969 m in domain 1, 455 m in domain 2 and 293 m in domain 3, the displacement across a domain is equal to (F_{xy}/F_{yy}) times the final width of the domain (for the values of F_{xy} and F_{yy} see equations 15a–c)), which represents a lower limit for the displacement since there may have been some rigid-body translation between domains 2 and 3, and the

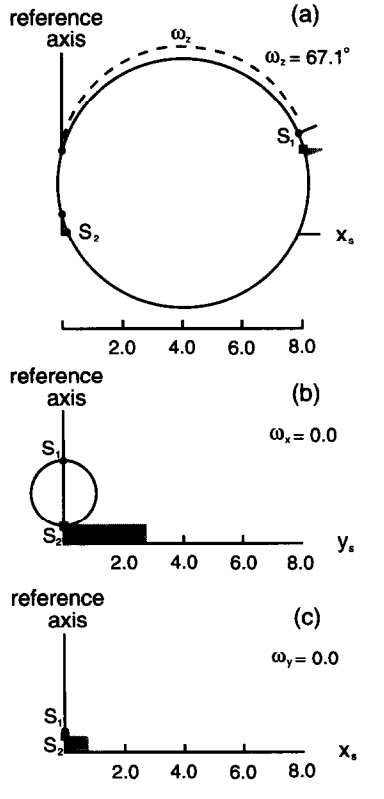

Fig. 13. Polar Mohr circles for domain 3 in (a) x_s–y_s, (b) y_s–z_s, (c) z_s–x_s planes in shear space. Legend as for Fig. 11.

amount of translation within the shear zone to the west of domain 3 is undetermined.

DISCUSSION AND CONCLUSIONS

Because fabrics in many natural shear zones are approximately symmetric about the plane common to the slickenline or stretching lineation and the pole to the shear plane, shear strains γ_{xz}, γ_{zx}, γ_{yz} and γ_{zy} are thought to be negligible in most cases. This geometrical condition requires that the components F_{xz}, F_{zx}, F_{yz} and F_{zy} of the position-gradient tensor must be zero. Strain analysis of deformed volcanic fragments from a shear zone in north-central British Columbia demonstrates that the errors arising from this assumption are negligible. Consequently, the position–gradient tensor is simplified to one which contains only five non-zero components.

Analysis of progressive strain may be used to determine the position–gradient tensor, provided deformation progresses under constant kinematics. The strain data obtained from our study area are incompatible with these conditions, presumably reflecting a change in the kinematics across the boundary between domains 2 and 3 or non-steady-state flow during the deformation.

An alternative method of determination of the position–gradient tensor from conventional strain data is based on the assumption that F_{yx} is negligible. This is valid for parallel-sided shear zones for which the kinematics are dominated by that for simple shear or simple shear combined with extension along the coordinate axes of shear space. It is clearly violated in 'general shear', in the sense of De Paor (1983) and Simpson & De Paor (1993), where the shearing falls into either the sub- or super-simple shear field. The assumption $F_{yx} = 0$ overestimates the rotational angle ω_z for sub-simple shear and underestimates the angle ω_z for super-simple shear. It should therefore be used cautiously in regions in which such a regime is suspected.

As discussed above, the assumptions that F_{xz}, F_{zx}, F_{yz} and F_{zy} are negligible are probably valid for many shear zones in nature. With these assumptions the position–gradient tensor **F** can be uniquely determined from the left stretch tensor **V**, which can be obtained by conventional strain analysis techniques. The deformation and rotation of lines and planes can then be readily studied either by tensor operations or by polar Mohr circle representations. As illustrated in this paper, once the **F** tensor is known, other features of the deformation, such as displacement on the boundaries or cumulative displacements across deformed zones, can be determined.

Acknowledgements—This research was made possible by grants from the British Columbia Ministry of Energy, Mines and Petroleum Resources, the Geological Survey of Canada and the Natural Sciences and Engineering Research Council. G. Z. was supported by a McGregor Scholarship during his doctoral research. Their support is gratefully acknowledged. We would like to express our appreciation to H. Fossen, W. Means, B. Tikoff and S. Wallis for their valuable comments and criticisms, which have improved the manuscript significantly.

REFERENCES

Allison, I. 1984. The pole of the Mohr diagram. *J. Struct. Geol.* **5**, 331–333.

Berthé, D., Choukroune, P. & Jegouzo, P. 1979. Orthogneiss, mylonite and non-coaxial deformation of granites: the example of the south Armorican shear zone. *J. Struct. Geol.* **1**, 31–42.

De Paor, D. G. 1983. Orthographic analysis of geological structures–I. Deformation theory. *J. Struct. Geol.* **5**, 255–277.

De Paor, D. G. & Means, W. D. 1984. Mohr circles of the first and second kind and their use to represent tensor operations. *J. Struct. Geol.* **6**, 693–701.

Elliott, D. 1970. Determination of finite strain and initial shape from deformed elliptical objects. *Bull. geol. Soc. Am.* **81**, 2221–2235.

Erslev, E. A. & Ge, H. 1990. Least-squares center-to-center and mean object ellipse fabric analysis. *J. Struct. Geol.* **12**, 1047–1059.

Flinn, D. 1979. The deformation matrix and the deformation ellipsoid. *J. Struct. Geol.* **1**, 299–307.

Fossen, H. & Tikoff, B. 1993. The deformation matrix for simultaneous simple shearing, pure shearing and volume change, and its application to transpression–transtension tectonics. *J. Struct. Geol.* **15**, 413–422.

Henry, B. 1990. Magnetic fabric implications for the relationship between deformation mode and grain growth in slates from the Borrowdale Volcanic Group in the English Lake District. *Tectonophysics* **178**, 225–230.

Hrouda, F. 1992. Separation of a component of tectonic deformation from a complex magnetic fabric. *J. Struct. Geol.* **14**, 65–71.

Hrouda, F. 1993. Theoretical models of magnetic anisotropy to strain relationship revisited. *Phys. Earth & Planet. Interiors* **77**, 237–249.

Jaeger, J. C. & Cook, N. G. W. 1979. *Fundamentals of Rock Mechanics*. Chapman & Hall, London and New York.

Malvern, L. E. 1969. *Introduction to the Mechanics of a Continuous Medium*. Prentice-Hall, New Jersey.

Means, W. D. 1976. *Stress and Strain: Basic Concepts of Continuum Mechanics for Geologists*. Springer, New York.

Means, W. D. 1982. An unfamiliar Mohr circle construction for finite strain. *Tectonophysics* **89**, T1–T6.

Means, W. D. 1983. Application of the Mohr-circle construction to problems of inhomogeneous deformation. *J. Struct. Geol.* **5**, 279–286.

Means, W. D. 1990. Kinematics, stress, deformation and material behavior. *J. Struct. Geol.* **12**, 953–971.

Owens, W. H. 1974. Mathematical model studies on factors affecting the magnetic anisotropy of deformed rocks. *Tectonophysics* **24**, 115–131.

Passchier, C. W. 1990. Reconstruction of deformation and flow parameters from deformed vein sets. *Tectonophysics* **180**, 185–199.

Passchier, C. W. 1993. The sliding-scale Mohr diagram. *Tectonophysics* **218**, 367–373.

Passchier, C. W. & Urai, J. L. 1988. Vorticity and strain analysis using Mohr diagrams. *J. Struct. Geol.* **10**, 755–763.

Pfiffner, O. A. & Ramsay, J. G. 1982. Constraints on geological strain rates: arguments from finite strain states of naturally deformed rocks. *J. geophys. Res.* **87**, 311–321.

Ramberg, H. 1975. Particle path, displacement and progressive strain applicable to rocks. *Tectonophysics* **28**, 1–37.

Ramsay, J. G. 1967. *Folding and Fracturing of Rocks*. McGraw-Hill, New York and San Francisco.

Ramsay, J. G. 1980. Shear zone geometry: a review. *J. Struct. Geol.* **2**, 83–99.

Ramsay, J. G. & Graham, R. H. 1970. Strain variation in shear belts. *Can. J. Earth Sci.* **7**, 786–813.

Ramsay, J. G. & Huber, M. 1983. *The Techniques of Modern Structural Geology*. Vol. 1. Academic Press, London and New York.

Rochette, P. 1988. Mathematical model relationship between the paramagnetic anisotropy and strain in slates—discussion. *Tectonophysics* **156**, 313–314.

Sanderson, D. J. 1982. Models of strain variation in nappes and thrust sheets: a review. *Tectonophysics* **88**, 201–233.

Sanderson, D. J. & Marchini, W. R. D. 1984. Transpression. *J. Struct. Geol.* **6**, 449–458.

Simpson, C. & De Paor, D. G. 1993. Strain and kinematic analysis in general shear zones. *J. Struct. Geol.* **15**, 1–20.

Tikoff, A. & Fossen, H. 1993. Simultaneous pure and simple shear: the unifying deformation matrix. *Tectonophysics* **217**, 267–283.

Treagus, S. H. 1990. The Mohr diagram for three-dimensional reciprocal stretch vs rotation. *J. Struct. Geol.* **12**, 383–395.

Twiss, R. J. & Gefell, M. J. 1990. Curved slickenfibers: a new brittle shear sense indicator with application to a sheared serpentinite. *J. Struct. Geol.* **12**, 471–481.

Weijermars, R. 1991. The role of stress in ductile deformation. *J. Struct. Geol.* **13**, 1061–1078.

Zhang, G. & Hynes, A. 1994. Fabrics and kinematic indicators associated with the local structures along Finlay–Ingenika fault, McConnell Creek area, north-central British Columbia. *Can. J. Earth Sci.* **31**, 1687–1699.

APPENDIX

Incremental $\mathbf{F}_i$ tensors for the strain paths of Fig. 5 are as follows:

$$\mathbf{F}_i^{(1)} = \begin{pmatrix} 1.0000 & 0.0600 & 0.0000 \\ 0.0000 & 1.0000 & 0.0000 \\ 0.0000 & 0.0000 & 1.0000 \end{pmatrix} \quad \text{(A1)}$$

$$\mathbf{F}_i^{(2)} = \begin{pmatrix} 1.0057 & 0.0593 & 0.0000 \\ 0.0000 & 0.9887 & 0.0000 \\ 0.0000 & 0.0000 & 1.0057 \end{pmatrix} \quad \text{(A2)}$$

$$\mathbf{F}_i^{(3)} = \begin{pmatrix} 1.0057 & 0.0603 & 0.0000 \\ 0.0000 & 1.0057 & 0.0000 \\ 0.0000 & 0.0000 & 0.9887 \end{pmatrix} \quad \text{(A3)}$$

$$\mathbf{F}_i^{(4)} = \begin{pmatrix} 0.9887 & 0.0603 & 0.0000 \\ 0.0000 & 1.0057 & 0.0000 \\ 0.0000 & 0.0000 & 1.0057 \end{pmatrix} \quad \text{(A4)}$$

$$\mathbf{F}_i^{(5)} = \begin{pmatrix} 1.0114 & 0.0597 & 0.0000 \\ 0.0000 & 0.9944 & 0.0000 \\ 0.0000 & 0.0000 & 0.9944 \end{pmatrix} \quad \text{(A5)}$$

$$\mathbf{F}_i^{(6)} = \begin{pmatrix} 0.9944 & 0.0607 & 0.0000 \\ 0.0000 & 1.0114 & 0.0000 \\ 0.0000 & 0.0000 & 0.9944 \end{pmatrix} \quad \text{(A6)}$$

$$\mathbf{F}_i^{(7)} = \begin{pmatrix} 0.9944 & 0.0597 & 0.0000 \\ 0.0000 & 0.9944 & 0.0000 \\ 0.0000 & 0.0000 & 1.0114 \end{pmatrix} \quad \text{(A7)}$$

$$\mathbf{F}_i^{(8)} = \begin{pmatrix} 1.0070 & 0.0594 & 0.0000 \\ 0.0000 & 0.9900 & 0.0000 \\ 0.0000 & 0.0000 & 1.0030 \end{pmatrix} \quad \text{(A8)}$$

$$\mathbf{F}_i^{(9)} = \begin{pmatrix} 0.9930 & 0.0606 & 0.0000 \\ 0.0000 & 1.0100 & 0.0000 \\ 0.0000 & 0.0000 & 0.9970 \end{pmatrix} \quad \text{(A9)}$$

where the superscripts show the path numbers.